RESEARCH

The Sun's Large-Scale Flows I: Measurements of Differential Rotation & Torsional Oscillation

Sushant S. Mahajan[1] · Lisa A. Upton[2] · H.M. Antia[3] · Sarbani Basu[4] ·
Marc L. DeRosa[5] · Shea A. Hess Webber[1] · J. Todd Hoeksema[1] · Kiran Jain[6] ·
Rudolf W. Komm[6] · Tim Larson[1] · Yury A. Nagovitsyn[7] · Alexei A. Pevtsov[6] ·
Thierry Roudier[8] · Sushanta C. Tripathy[6] · Roger K. Ulrich[9] · Junwei Zhao[1]

Abstract

We have developed a comprehensive catalog of the variable differential rotation measured near the solar photosphere. This catalog includes measurements of these flows obtained using several techniques: direct Doppler, granule tracking, magnetic pattern tracking, global helioseismology, as well as both time-distance and ring-diagram methods of local helioseismology. We highlight historical differential rotation measurements to provide context, and thereafter provide a detailed comparison of the MDI-HMI-GONG-Mt. Wilson overlap period (April 2010 – Jan 2011) and investigate the differences between velocities obtained from different techniques and attempt to explain discrepancies. A comparison of the rotation rate obtained by magnetic pattern tracking with the rotation rates obtained using local and global helioseismic techniques shows that magnetic pattern tracking measurements correspond to helioseismic flows located at a depth of 25 to 28 Mm. In addition, we show the torsional oscillation from Sunspot Cycles 23 and 24 and discuss properties that are consistent across measurement techniques. We find that acceleration derived from torsional oscillation is a better indicator of long-term trends in torsional oscillation compared to the residual velocity magnitude. Finally, this analysis will pave the way toward understanding systematic effects associated with various flow measurement techniques and enable more accurate determination of the global patterns of flows and their regular and irregular variations.

1. Introduction

Solar magnetic activity is caused by the complex interaction between the Sun's flows and the evolving magnetic field. At the largest scales, this takes the form of the solar dynamo. In 1955, Eugene Parker (Parker, 1955) derived a set of equations showing that non-axisymmetric lifting and twisting of magnetic field by convective motions could generate an oscillating magnetic field. A few years later, H.W. Babcock proposed a phenomenological description of how the dynamo process could explain many observed characteristics of

---

Extended author information available on the last page of the article

the solar cycle (Babcock, 1961). This description included four key stages: (a) the Sun starts with a dipole poloidal magnetic field embedded through the convection zone; (b) differential rotation shears the magnetic field and transforms it into a toroidal field configuration; (c) the toroidal field gets stronger, becomes buoyant, and the fields then emerge as active regions with a systematic tilt; and (d) surface flux transport causes the field to cancel, preferentially across the equator, and the excess polarity magnetic flux is transported to the poles, where it reverses the initial poloidal field and builds a new poloidal magnetic field with the opposite polarity. NASA has funded a DRIVE Science Center specifically charged with studying and improving our understanding of the Consequences Of Fields and Flows in the Interior and Exterior of the Sun (COFFIES: coffies.stanford.edu). One of the key objectives of COFFIES is to develop a comprehensive catalog of the time-evolving large-scale near-surface flow: differential rotation and meridional flow. This catalog will be used to constrain the global flow patterns and their regular and irregular variations during the solar magnetic cycle.

In this paper we present several measurements of the solar differential rotation and our findings based on these measurements. During the course of writing this paper, we noted that particular terminology related to differential rotation and its variability has different meanings or context among the scientific community. For this reason, we explicitly define the following terms as they are used in this paper:

- *Differential Rotation:* The overall rotation rate of the Sun around its axis that varies with latitude, depth, and time. This is typically a longitudinal average of rotation rate and can be reported in the sidereal, synodic, or Carrington frame (with a constant sidereal rotation period of 25.38 days subtracted) in any velocity (e.g., $m\,s^{-1}$) or frequency unit (e.g., nHz).
- *Mean Differential Rotation:* A solar rotation rate profile constructed as a function of only latitude, or latitude and depth by the longitudinal and temporal averaging of long-term rotation-rate measurements. It can be in sidereal, synodic, Carrington or Snodgrass frame (Snodgrass, 1984) and in any velocity (e.g., $m\,s^{-1}$) or frequency unit (e.g., nHz).
- *Torsional Oscillation (TO):* The time-varying, residual component of solar rotation, which is calculated by subtracting the mean differential rotation from differential rotation. This can be reported as a function of latitude, depth and time. It can be in units of velocity or frequency. This may also be known as *zonal flow* or *residual differential rotation*, but for this paper we use the term *Torsional Oscillation*.
- *Sunspot Belt:* The locations on the solar photosphere where a bulk of sunspots appear. This is determined by marking the extrema of sunspot latitudes independently in northern and southern hemisphere as a function of the phase of the sunspot cycle. These extrema of sunspot latitudes are later smoothed in time using an annual running mean.

We analyze data provided by four different Doppler magnetograph instruments, two of which are ground-based and two of which are space-based. Ground-based observations are obtained from Mount Wilson Observatory (MWO: Howard et al., 1983b; Ulrich et al., 1991; Ulrich, Tran, and Boyden, 2023) and the Global Oscillation Network Group (GONG: Harvey et al., 1996; Harvey, Tucker, and Britanik, 1998). MWO data used in this study are obtained from the Fe I 5250.2 Å fast-scan program described in Ulrich et al. (1988), which put together several 34×34 pixel arrays to scan the solar disk daily since the year 1983. The GONG instrument, on the other hand, uses the Ni I 6767.8 Å line and has a resolution of $5''$ Nyquist sampled at $2.5''$ per pixel. The GONG project began operations in 1995 and still continues to operate. The space-based Michelson Doppler Imager (MDI: Scherrer et al., 1995) onboard *Solar and Heliospheric Observatory (SOHO)* observed the Sun using Ni I 6767.8 Å photospheric spectral line at five different filter tunings in order to infer the line-of-sight Doppler velocity and magnetic flux density with a resolution of $4''$ Nyquist sampled

at 2″. Whereas the Helioseismic and Magnetic Imager (HMI, Scherrer et al., 2012; Schou et al., 2012) onboard *Solar Dynamics Observatory (SDO)* observes the Fe I 6173 Å line in six different filters and polarizations to infer the Doppler velocity and magnetic field with a resolution of 1″ Nyquist sampled at 0.5″.

We begin with a brief history of differential rotation in Section 2. Section 3 provides a summary of the modern measurement techniques used to obtain the flows described in this paper. Section 4 shows the differential rotation profiles obtained using these techniques during the time of overlapping measurements for all four of the instruments used to obtain these flows. In Section 5 we compare the TO pattern for Solar Cycles 23 and 24 using different measurement techniques.

2. Classic Measurements of Solar Differential Rotation

2.1. Sunspot Tracking

Since their discovery, sunspots have been extensively used as tracers of solar rotation. Galilei, Welser, and de Filiis (1613) announced the fact of solar rotation, and Scheiner (1630) estimated the elements of Sun's rotation, including its period (27 days) and 7° inclination angle of solar rotation axis to the ecliptic. Scheiner also found that some sunspots were able to complete a full rotation in 25 days (near the solar equator), while others (at higher latitudes) took closer to 28 days (e.g., Mitchell, 1916). This led him to the realization that the Sun's rate of rotation depends on latitude, i.e., the Sun rotates differentially. In the late 1850s, Richard C. Carrington also tracked and recorded the motions of sunspots on the Sun (Carrington, 1859). He determined that the rotational axis of the Sun was tilted by about $\sim 7.25°$ with respect to the ecliptic. In order to create a standard of reference, Carrington calculated the average synodic (as viewed from the Earth orbiting the Sun) rotation rate of the Sun. A full synodic rotation of the Sun (27.2753 days) is now known as a Carrington Rotation. In the late 19th century, an expression for the differential rotation began to emerge, e.g., see Adams (1911), Belopolsky (1933). This expression, known as Faye formula, characterizes the angular (sidereal) rotation rate, ω, typically in the form of:

$$\omega(\lambda) = A + B \sin^2 \lambda, \tag{1}$$

where λ is the latitude. Table 1 shows the differential rotation coefficients for the Faye formula from several observers between 1853 and 1932. These early observations provided a robust determination of solar-rotation profile with latitude. It was shown that the rotation profile is symmetric relative to the equator, plages and sunspots exhibit similar rotation rates, and the rotation rate changes with age of sunspot groups. Spectral observations showed the change in rotation with height in solar atmosphere.

Newton and Nunn (1951) measured the rotation rate of sunspots from 1934 to 1944 (i.e., Solar Cycle 17) using the sunspot record of the Royal Greenwich Observatory. They found a sidereal rotation rate with the coefficients $A = 14.38°$ day^{-1} and $B = 2.96°$ day^{-1}. Their measurements were in good agreement with those of Carrington (though it included a difference in the functional form, see Table 1). They compared these results to measurements from the prior five solar cycles and found no apparent variation from one cycle to the next nor over the solar cycle itself. They also noted that the differential rotation was symmetric across the equator, i.e., no hemispheric difference was seen.

Table 1 Differential rotation coefficients from historical measurements (modified from Belopolsky 1933, Delury 1939).

No.[1]	Reference	Function ($\omega =$)	Epoch	Method[2]
1*	Carrington	$14.42 - 2.75 \sin^{7/4} \lambda$	$1853 - 1861$	T
2*	Spörer	$8.53 + 5.80 \cos \lambda$	$1860 - 1870$	T
1	Carrington/fitted by Faye	$14.37 - 3.10 \sin^2 \lambda$	$1853 - 1861$	T
2	Spörer/fitted by Faye	$14.37 - 3.28 \sin^2 \lambda$	$1860 - 1870$	T
3	Maunder	$14.44 - 2.01 \sin^2 \lambda$	$-$	T
4	Newton	$14.37 - 2.60 \sin^2 \lambda$	$1878 - 1923$	T
5	Newton	$14.37 - 3.00 \sin^2 \lambda$	$1924 - 1933$	T
6	Stratonov	$14.51 - 2.66 \sin^2 \lambda$	$1881 - 1884^3$	T
7	Dunér	$15.41 - 4.81 \sin^2 \lambda$	$1888 - 1901$	S
8	Halm	$14.53 - 2.50 \sin^2 \lambda$	$1901 - 1903$	S
9	Adams	$14.54 - 3.50 \sin^2 \lambda$	1908	S
10	Storey and Wilson	$14.75 - 3.20 \sin^2 \lambda$	1909	S
11	Plaskett	$14.37 - 4.00 \sin^2 \lambda$	1911	S
12	Hubrecht	$13.23 - 3.20 \sin^2 \lambda$	1911	S
13	Schlesinger	$14.17 - 3.40 \sin^2 \lambda$	1912	S
14	De Lury	$14.04 - 4.00 \sin^2 \lambda$	1915	S
15	Belopolsky	$13.90 - 3.67 \sin^2 \lambda$	1927	S
16	Freundlish and Brück	$13.43 - 2.88 \sin^2 \lambda$	1930	S
17	Belopolsky	$13.74 - 3.69 \sin^2 \lambda$	1932	S

[1] * marks original functional dependencies fitted by Carrington and Spörer.

[2] T - sunspot/plage tracking, S - spectroscopy.

[3] As fitted using faculae data from Stratonoff (1896).

Later observations showed that, in fact, there were changes in the differential rotation.[1] Howard, Gilman, and Gilman (1984) measured sunspot positions and areas from white light images of the Sun captured on photographic plates by MWO from 1921 to 1982. They found that the rotation rate as measured by tracking sunspot groups was slower ($\sim 1\%$) than as measured by tracking individual spots. Furthermore, the rotation rate measured by tracking larger spots was slower ($\sim 2\%$) than smaller spots. A similar result was recently obtained by Jha et al. (2021) using the newly digitized Kodaikanal Solar Observatory sunspot data from 1923 to 2011. Hathaway and Wilson (1990) showed that these relationships translated into a small ($< 5\%$) solar-cycle variation of the differential rotation as measured by the motion of sunspots as they transit the Sun.

Determination of solar differential rotation using sunspot tracers may be subject to several systematic errors. For example, as active regions evolve, individual sunspots may exhibit proper motions, including leading and following polarities moving away from each other as active regions grow. Thus, tracking individual spots may result in slight faster/slower rotation rate, when using leading/following spots. Averaging solar rotation derived from feature tracking over extended ranges of latitude may show a velocity pattern similar to torsional os-

---

[1] Changes in the solar rotation rate were noted much earlier, see, e.g., Figure 3 in Belopolsky (1933), showing changes in solar rotation from $1895 - 1932$.
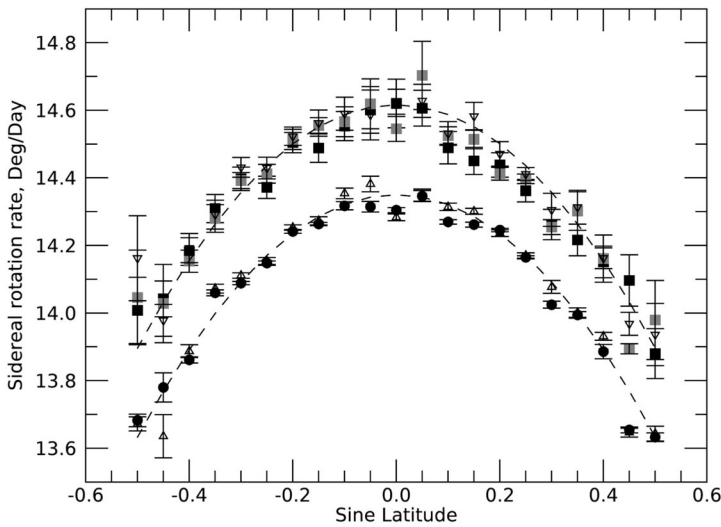
Figure 1 Solar rotation for small short-lived (SSGs, filled black and gray squares, upside open triangles) and large long-lived sunspot groups (LLGs, filled circles, and open triangles). Adapted from Nagovitsyn, Pevtsov, and Osipova (2018). Dashed curves correspond to Equations 2 and 3.

cillation (see Section 5.2). Tlatov and Pevtsov (2013) have demonstrated that as the sunspot activity shifts from higher to lower latitudes in course of solar cycle, the average velocity computed over the pixels with large extension in latitude would be skewed by changes in weighting function as darker features (e.g., sunspots, pores) gradually move across range of latitudes covered by a pixel. This would create a pattern of faster-slower rotating bands, reminiscent of torsional oscillation pattern. This is further complicated by the fact that the rotation from tracking sunspots and other features (e.g., coronal bright points) is different for features of different size and lifetime (e.g., Lamb, 2017; Nagovitsyn, Pevtsov, and Osipova, 2018). Figure 1 shows sidereal rotation for small short-lived (SSGs) and large long-lived sunspot groups (LLGs). For SSGs (upper curve), the mean rotation profile corresponds to

$$\omega = (14.616 \pm 0.013) - (2.88 \pm 0.13) \sin^2 \lambda. \tag{2}$$

For LLGs,

$$\omega = (14.3499 \pm 0.0039) - (2.86 \pm 0.043) \sin^2 \lambda. \tag{3}$$

For additional explanation see Nagovitsyn, Pevtsov, and Osipova (2018, 2023b).

2.2. Doppler Measurements

Direct Doppler (DD) measurements provide an indication of the plasma motion along the line-of-sight in the Sun's photosphere based on the Doppler shift of spectral lines. While measurements made by tracking sunspots are restricted to active latitudes, Doppler measurements can be made at all latitudes. The 150-feet tower telescope at the MWO was the first system to obtain digital maps of the Sun's magnetic fields and Doppler shifts through the operation of the system described by Babcock (1953). The development and use of the
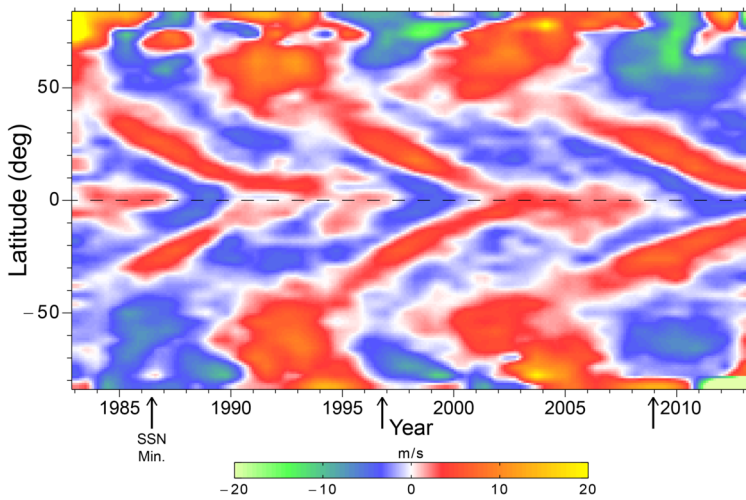
Figure 2 Torsional oscillation for the period 1983 to 2012, derived using Direct Doppler measurements from MWO.

magnetograph in these measurements were described by Howard (1965), Howard, Tanenbaum, and Wilcox (1968), Howard (1974), Howard (1976), and Howard et al. (1983b) with the calculation of rotation velocities being given by Howard and Harvey (1970). Howard and Labonte (1980) measured the rotation rate using Doppler images from MWO. They characterized the rotation rate for each Carrington rotation with three coefficients A, B, and C such that the angular rotation rate (ω) is given by

$$\omega(\lambda) = A + B \sin^2 \lambda + C \sin^4 \lambda. \tag{4}$$

The long duration of the MWO observations implies that they can provide a guide for the interpretation of results from ongoing helioseismic observations. Howard and Labonte (1980) calculated the average rotation rate at each latitude (λ) and subtracted this from the rotation rate measured for each rotation. They then plotted the residual rotation as a function of time for the interval from January 1968 to December 1979 and found an oscillating pattern in the residual rotation rate, which they referred to as *torsional oscillation*.[2] The excess velocities (with magnitudes of $\sim 3 \, \mathrm{m \, s^{-1}}$ or $\sim 1\%$ of the rotation rate) created a chevron-like pattern that alternates between slower and faster zones with a period of about 11 years.

Howard et al. (1983b) described the data system installed at MWO at the end of 1982. The last system upgrade was the installation of the 24-channel system in 1991 (Ulrich et al., 1991) that provided nine spectral band-pass pairs that can be used in the magnetogram/Dopplergram mode. The pre-1983 data had calibration issues that made inclusion of the older data problematic. Figure 2 shows the torsional oscillation for the period 1983 to 2013 (Ulrich, Tran, and Boyden, 2023). These measurements are from a reduction using a new algorithm that imposes two restrictions: 1) the absolute value of the sine of the central

---

[2]Earlier, Chistiakov (1976) used the same term to describe deviations of solar rotation from the average differential rotation profile. He averaged the deviations over each hemisphere separately, and thus, did not observe a chevron-like pattern discovered by Howard and Labonte (1980).

meridian distance, ϕ, is kept less than 0.85 and 2) the absolute value of the magnetic field for the observed pixel must be less than 30 G. The new algorithm also fits the limb shift along an equatorial band $\pm 4°$. Each image is divided into bins $4°$ wide and the line-of-sight velocities in each bin are fitted to a quadratic function of $\sin(\phi)$. The coefficients in this fit, (α and β), give the meridional velocity times $R_\odot[\sin(\phi)\cos(B_0) - \cos(\phi)\sin(B_0)]$ and the rotational velocity, while γ provides the freedom to fit α and β. In the formula for the meridional velocity, B_0 is the angle of the sun's rotation axis relative to the line-of-sight.

The annual valatexriation in viewing angle due to the Sun's rotation axis being out of the ecliptic creates intervals when the highest latitudes are not visible, and these are assigned a null value. These null values have been replaced by spline fit values. Plotted values are from six Carrington rotation bins of the observations. We note the following: 1) the speedup and slowdown bands are largely continuous over time between when a band appears until the band disappears near the equator, 2) there are long intervals when the band with the slow-down persists with little migration, 3) the transitions between slowdown and speedup and vice versa are abrupt.

3. Modern Measurement Techniques

In the last few decades, helioseismology (HS) has revealed a great deal about the internal structure of the Sun, including the variation of rotation rate through the solar convection zone. Thompson et al. (1996) applied helioseismology techniques to data obtained with GONG to determine that the rotation rate increases down to a depth of about $0.95R_\odot$. This region from the photosphere to $0.95R_\odot$ is known as the *near-surface shear layer*. At a depth of about $0.7R_\odot$, i.e., the base of the convection zone, the rotation rates at different latitudes merge and the Sun rotates nearly like a solid body interior to that depth. A second shear layer is present in this transitionary region, known as the *tachocline*. These results have been confirmed by Schou et al. (1998) using MDI data. Helioseismic inversions of rotation rate in the solar interior also confirmed the existence of TO in the measured flow velocities and showed that TO extends deep into the convection zone (Howe et al., 2000; Vorontsov et al., 2002). Furthermore, several other measurement techniques have been developed to measure plasma flows directly or indirectly using certain features as tracers of plasma flows (e.g., sunspots, large scale magnetic patterns, supergranules). Each of these techniques comes with its pros, cons, and systematic errors, some of which are not well known.

This section provides a brief description of the techniques used to measure the differential rotation that are compared in this paper. In Table 2 we list these techniques, define an abbreviation used to refer to them in this paper, the instruments used to obtain the data, the spatial resolution, the cadence, observational period, and the associated references. While there certainly are more techniques for measuring the differential rotation of the Sun than those included in this paper, we use the ones that have readily available data during the last two solar cycles. A comparison of differential rotation rates obtained from these techniques is discussed in Section 4 and a comparison of the TO during Solar Cycles 23 and 24 is discussed in Section 5.

3.1. Global Helioseismology

Global-mode helioseismology relies on the decomposition of solar images into their spherical harmonic components, which are characterized by degree ℓ and azimuthal order m. A third integer, the radial order n, characterizes the radial eigenfunctions. Modes described by

Table 2 The flow measurement techniques presented in this study. This table lists the various techniques described in this paper, their abbreviation, the source of the data used, resolution, averaging period, observing interval, and references. Techniques marked with a † are forced to be symmetric across the equator. 'CR' denotes velocity averages over a Carrington rotation (27.2753 days).

Measurement Technique	Abrev.	Instrument	Resol.	Avg. period	Obs. Interval	References
Global HS	GHS1†	GONG	2.00°	36 days	1995–2021	Antia, Basu, and Chitre (2008)
Global HS	GHS2†	MDI, HMI	2.00°	72 days	1995–2022	Larson and Schou (2018)
Global HS	GHS3†	MDI, HMI	2.00°	72 days	1995–2022	Antia and Basu (2022)
Ring Diagram HS	RD1	GONG	7.50°	CR	04/22/2010–01/20/2011	Corbard et al. (2003)
Ring Diagram HS	RD2	MDI, GONG, HMI	7.50°	CR	2002–2021	Bogart et al. (2011a,b)
Time–Distance HS	TD	HMI	0.12°	CR	2010–2022	Zhao et al. (2012b)
Direct Doppler	DD†	MWO	3.37°–7.21°	CR	1996–2013	Ulrich et al. (1988)
Granule Tracking	GT†	HMI	5°	CR	08/16/2010–09/14/2010	Roudier et al. (2018)
Magnetic Pattern Tracking	MPT1	MDI, HMI	0.70°	CR	1995–2022	Hathaway, Upton, and Mahajan (2022)
Magnetic Pattern Tracking	MPT2	MDI, HMI	4.39°	CR	1995–2021	Mahajan et al. (2021)

n, ℓ, and m each have their own frequency, but this is typically parameterized by a mean multiplet frequency for each ℓ and n, while the frequency variation with m is described by a polynomial, resulting in the so-called a-coefficients (Schou, Christensen-Dalsgaard, and Thompson, 1994). A spherical harmonic analysis is complicated by the fact that because we cannot see the entire Sun, modes cannot be perfectly separated and they leak power into the spectra for different spherical harmonics. We use global helioseismic inversions of differential rotation from two sources, as described below.

3.1.1. GONG (GHS1)

Dopplergrams from the six GONG sites are decomposed into spherical harmonic time series up to a maximum degree of ℓ=200 and then merged to form timeseries 108 days long with start dates spaced 36 days apart. Hence, there is a considerable overlap between neighboring data sets. The timeseries are detrended by first-differencing, and the power spectrum is fit for each n, ℓ and m separately. Leakage is not taken into account, and a-coefficients are derived afterwards by fitting polynomial functions to the individual-m frequencies within each multiplet. Oscillation frequency data sets are available from the GONG website gong.nso.edu.

Each 108-day long GONG data set is inverted to calculate the angular rotation rate, $\omega(r, \lambda)$ as a function of radius and latitude, using the 2D Regularized Least Squares (RLS) technique, described by Antia, Basu, and Chitre (1998, 2008). The frequency splittings of the global p modes are sensitive to only the north–south symmetric component of the rotation rate, so it is not possible to infer the antisymmetric component. The temporal variation in ω is obtained by using different 108-day long data sets. This work includes 259 such data sets covering the period from 7 May 1995 to 25 January 2021 with a latitudinal resolution of $2°$ covering the depth range $0.68R_\odot$ to $1.00R_\odot$ with a resolution of $0.02R_\odot$.

3.1.2. MDI-HMI (GHS2 & GHS3)

GHS2:

Due to telemetry constraints, most of the time the MDI Dopplergrams are reduced in resolution onboard the spacecraft. In particular, they are smoothed with a Gaussian and subsampled by a factor of five in each direction, and then cropped to 90% of the image radius.

Once on the ground, the Dopplergrams are corrected by subtracting the orbital velocity of the spacecraft, as well as models of convective blueshift and differential rotation. They are apodized in fractional image radius from 0.83 to 0.87 and then decomposed up to a maximum degree of ℓ=300. The resulting components are formed into non-overlapping timeseries 72 days long, and each timeseries is detrended by polynomial subtraction and gap-filled using an auto-regressive algorithm before undergoing a Fourier transform. For each ℓ and n, the transforms are fit using a maximum likelihood approach that yields, among other parameters, a mean multiplet frequency and six a-coefficients directly, which allows f-modes to be fit. Mode leakage caused by geometric effects, Gaussian smoothing, and coupling by differential rotation are taken into account, and the fit is iterated ten times. On the final iteration, 18 and 36 a-coefficients are also fit. For this work, the 36 coefficient fits are inverted using a 2D RLS technique with two independent penalty terms given by integrals over the square of the second derivative of the rotation rate in each direction (Schou, Christensen-Dalsgaard, and Thompson, 1994). Radial and latitudinal trade-off parameters used are 10^{-6} and 10^{-2}, respectively.

For the sake of continuity, the HMI Dopplergrams are used to create a proxy for the MDI low-resolution data. This is done by binning them by a factor of four and then convolving and subsampling them as described for MDI. The resulting Dopplergrams are processed exactly like those from MDI. During the overlap period, for this paper the HMI data were used. For further details, see Larson and Schou (2015, 2018).

These rotation inversions are available from JSOC (jsoc.stanford.edu) in dataseries mdi.vw_V_sht_2drls and hmi.vw_V_sht_2drls from 1 May 1996 up to 16 Aug 2022. The value of the VERSION keyword for the data used here is "version2". When plotting these inversions below, the MDI rotation rates are matched to the HMI values by cross-calibrating them during their overlap period. To enable direct comparison with GHS1, we interpolated these inversions onto the same grid in latitude and depth.

It should be noted that this analysis contains known systematic errors that are not present in the analysis of full disk data from either MDI or HMI. However, the difference these errors make to inversions is mostly confined to high latitudes and is not visible at the scale investigated here.

GHS3: We also include here a global helioseismic rotation inversion dataset derived from MDI and HMI data using the 2DRLS inversion technique described in Section 3.1.1 for GHS1. This dataset is synchronized in time with GHS2, with 72 day non-overlapping rotation rate averages.

3.2. Local Helioseismology

3.2.1. Ring Diagram Analysis (RD1 and RD2)

The ring-diagram helioseismology technique (Hill, 1988) produces a three-dimensional power spectrum (two in space and one in time) of a localized region on the surface of the Sun, which is remapped and tracked over a given time period. For the analysis of this spectrum, we use helioseismic inversion products based on full-disk Dopplergrams obtained with the MDI dynamics program, the GONG network, and the HMI instrument. The MDI dynamics program data covered about two months (up to three) of a given calendar year due to telemetry constraints.

The horizontal components of solar subsurface flows are determined using the dense-pack tiles developed originally for MDI data (Haber et al., 2000) which was subsequently adapted to GONG data (Corbard et al., 2003) and finally to HMI data (Bogart et al., 2011a,b). The dense-pack tiles are evenly spaced in latitude and longitude with their centers separated by 7.5°. These tiles do not cover the entire Sun, but extend to a pre-defined distance from the disk center, depending on the spatial resolution of the instrument. Since the analyzed regions are circular with 15° diameter, the dense-pack regions at neighboring grid points overlap and the flow inferences are not fully independent for each region.

To study temporal variations, we combine daily flow maps to form synoptic flow maps and then average the synoptic maps in longitude to form super-synoptic maps. The daily flow maps from GONG and HMI Dopplergrams were obtained from their respective ring-diagram pipelines; the daily MDI flow maps were provided by D. Haber. The synoptic maps are calculated on a longitude–latitude grid with centers spaced by 7.5° ranging over $\pm$ 52.5° (MDI and GONG) and $\pm$ 67.5° (HMI) in latitude and covering 16 depths from 0.6 to 15.8 Mm. Daily HMI flow maps can cover up to 75° in one hemisphere, if the solar inclination toward the Earth or B_0 angle is favorable.

We correct the horizontal flows for systematic variations with disk position, which can be modeled as center-to-limb variations of solar and instrumental origin (Baldner and Schou,

2012). Komm et al. (2015) found that the north-south variation of the zonal flow consists of a constant nonzero component in addition to the annual variation and thus indicated a geometric projection artifact. One of the methods to remove these systematic effects is described in the same paper. However, an offset still remains between the zonal flows derived from GONG and HMI data; the offset and its standard deviations are 1.5 ± 2.5 ms^{-1} averaged in depth (Komm, Howe, and Hill, 2018).

The dataset RD1 consists of rotation rates obtained from GONG data using 30° tiles at latitudinal resolution of 7.5° and averaged over the interval 22 April 2010 to 20 Jan 2011, which is essentially the period of overlap when MDI, HMI, GONG, and MWO were all simultaneously operating. These are available at depths of 0.74, 0.90, 1.90, 20.60, 24.80, and 29.70 Mm inside the Sun.

The dataset RD2, on the other hand, consists of rotation inversions obtained from GONG, MDI and HMI data using 15° tiles with the same latitudinal resolution 7.5°, but with a cadence of 27.2753 days (every CR). Here we use MDI dynamics program data covering 29 Carrington rotations which sparsely populate the interval CR 1909 – 2020 (i.e. 23 May 1996 – 30 August 2004). The GONG data used cover 261 consecutive Carrington rotations from CR 1979 – 2239 (22 July 2001 – 12 January 2021), while the HMI data were obtained during 146 consecutive Carrington rotations, CR 2097 – 2242 (2 May 2010 – 14 April 2021). Note that for analyzing temporal variations, both GONG and MDI flow values are scaled to match HMI values. However, for the analysis of acceleration in Section 5.2, we ignore the MDI dynamics program data prior to 22 July 2001 due to its sparse nature.

3.2.2. Time–Distance Helioseismology (TD)

While ring-diagram analysis performs ridge fittings in the Fourier domain of the solar oscillation data, time-distance helioseismology (Duvall et al., 1993) measures acoustic travel times between different surface locations in the space and time domain. The acoustic waves travel in the solar interior along curved paths, and their travel times from one location to another are altered by subsurface sound-speed perturbations and flows. Subsurface flows can be inverted by solving a set of equations that relate the flows with the travel-time measurements through sensitivity kernels (Kosovichev, 1996).

In this paper, we use flows obtained from the HMI time-distance helioseismic data-analysis pipeline (Zhao et al., 2012b), which generates near-real-time subsurface flow–fields every 8 hours with a spatial sampling of 0.12°. These subsurface flow–fields cover most of the solar disk with an area of $123° \times 123°$, with depths from the photosphere to approximately 20 Mm. We only use the near-surface results (0 – 1 Mm) from this pipeline for this work.

For each Carrington rotation, we average subsurface flow–fields for the east–west and north–south directions at the selected depth, and obtain the averaged differential rotation and meridional flow profiles as functions of latitude. The average is performed along a 30°-wide central meridian band, so that the systematic center-to-limb effect in the meridional-flow measurements can be readily removed following the prescription by Zhao et al. (2012a). The differential rotation is then ready for use after averaging over every CR. The reduced data are available from doi.org/10.25740/ph433nq0725.

3.3. Direct Doppler

Obtaining a solar rotation law using spectral-line Doppler shift is complicated by a number of issues. Terrestrial atmospheric blurring (seeing) and telescope optical and atmospheric

scattering mixes light from different parts of the solar image so that the derived Doppler shift, especially near the limb, is altered. The formation of the spectral feature in the solar atmosphere is complicated by a number of instrumental and physical processes that influence the position of the line – convective motions at the granulation and supergranulation scale, pressure-induced shift, meridional circulation shift, magnetic fields, and solar rotation.

The 150-feet tower telescope on Mt. Wilson has yielded the Doppler shift velocities of the Fe I line at a wavelength of 5250.2 Å as product of the Babcock magnetograph (Babcock, 1953) series of magnetic field observations covering the interval from 1967 to 2013. Reduction of the data has followed the methods described by Howard and Harvey (1970), Howard (1976), Howard, Boyden, and Labonte (1980), Howard et al. (1983a,b), Ulrich et al. (1988, 1991, 2002), Ulrich, Tran, and Boyden (2023). The primary corrections are the removal of a fit to the limb-shift function derived from a band along the equator between $\pm 4°$ of latitude. In addition, pixels having a magnetic–field in excess of 30 G were dropped. The limb-shift function has been discussed extensively and is dependent on choice of spectral line and adopted spectral sampling bands (Beckers and Nelson, 1978; Dravins, Lindegren, and Nordlund, 1981; Labonte and Howard, 1982b; Ulrich et al., 1988). The differential rotation is fit to the A, B, C coefficients of Equation 4, which accounts for the non-varying component of rotation.

A general problem in the study of large-scale and long-lived velocities on the solar surface is the impact of motions from the supergranulation. The impact of supergranular velocities is large compared to the rotational and meridional variations and this impact can only be mitigated through averaging. The lifetime of the supergranulation is of order one day, so this averaging must extend over many days. The effect of the supergranulation shows up in all three rotation coefficients. Scattered light variations impacted the earlier reduction values of A, but are not a factor in the most recent reductions by Ulrich, Tran, and Boyden (2023). The B and C coefficients also vary from one observation to the next, but do show a solar-cycle effect, so that care is needed to avoid leaving some variation in B and C with the remainder left in the derived TO deviations. For the full horseshoe curve, we use the average over all observations. Because the form of the series solution is not based on a physical necessity, a lively debate ensued in the publications by Labonte and Howard (1982a) and Snodgrass and Howard (1985) concerning the high latitude oscillation behavior. Following the plan given by Ulrich et al. (1988), the MWO project now avoids this uncertainty by holding the B and C coefficients fixed in time (with $B = -0.409999$ and $C = -0.418867$) and leaving the variations at each latitude dependent deviations that we can average over.

For analyzing the mean differential rotation obtained from MWO rotation A coefficients, we averaged the rotation rate measured during the overlap period with other instruments: CR 2096 to CR 2105. These rotation A coefficients are listed in Table 3 in the Appendix and these data are used in Section 4. Furthermore, for the analysis of the torsional oscillation pattern (Section 5), we used velocity measurements from the Fe I 5250.2 Å line, which forms closest to the photosphere among the selection of available lines from MWO. These direct velocity measurements are available as Carrington rotation averages from 18 August 1996 up to 24 November 2012 with a variable resolution in latitude (3.37° near equator to 5.96° at high-latitudes). The magnetic, Doppler and intensity values are also available in fits format from gonewithsolarwind.com/index.php/full-disk-observations-from-the-third-generation-magnetograph-at-mwo/.

3.4. Granule Tracking (GT)

A coherent structure tracking analysis (CST: Roudier et al., 2012) can be performed on photospheric structures, such as granules, which act as passive tracers. The CST method measures the velocities by following the trajectory of each granule, *i.e.*, solar plasma, during the life of the coherent object, which is defined by its appearance and disappearance if the granule does not split or merge. The velocity induced by the time evolution of B_0 (i.e., the tilt of the solar North rotational axis toward the observer), the motion of the satellite, and limb effects are corrected. Applying this procedure to HMI data, a sequence of velocity-field maps with temporal resolution of 30 min and a spatial resolution of 2.5 Mm can be obtained. This technique provides the photospheric velocity field (u_x, u_y) in the plane of the sky. Combining these components with line-of-sight Doppler data that provides u_z, one can calculate the full vector velocity at the surface in solar spherical coordinates, (u_r, u_λ, u_ϕ), where λ is the latitude and ϕ the longitude. Different measures of solar differential rotation and meridional flow have been published using this technique (Roudier et al., 2012, 2013, 2018), up to high latitudes with low noise.

A comparison of solar rotation measurements made on the same day (4 June 2019; quiet Sun) with a B_0 close to 0 ($B_0 = -0.31°$), between the Doppler data and the CST measurements (solar granule tracking) shows:

i) A systematic difference of the rotation velocity obtained with the CST relative to the rotation measurements using only the Doppler component (classical measurement) of about 170 ms^{-1} in the sidereal reference frame. The equatorial rotation obtained from CST is smaller than the reference spectroscopic profile computed from Dopplergrams.
ii) There is a slight underestimation of rotational velocities above 30° latitude due to the projection effects on the solar granules.

The CST technique measures the proper motion of structures visible in intensity, averaged over a spatial and temporal window. It is an indirect and average measurement. The solar rotation amplitude obtained from the u_ϕ component is normalized to the solar rotation obtained from Doppler measurements. The segmentation of the structures in intensity is one of the sources of the underestimation of the u_x and u_y velocities in the plane of the sky. However, the amplitude of this underestimation is quite stable, regardless of the spatial and temporal windows or sequences used. The different CST parameters tested also do not show great influence in the range commonly used in the data reduction (Roudier et al., 2012, 2013, 2018). This makes it easier to normalize the amplitude of u_x and u_y relative to the Doppler amplitude.

3.5. Magnetic Pattern Tracking (MPT1 & MPT2)

Hathaway and Rightmire (2010, 2011) developed a magnetic pattern tracking algorithm (MagTrak) to measure the differential rotation and meridional flow in SOHO/MDI magnetograms. Rather than track the motion of individual features (e.g., sunspots, granules, magnetic elements), MagTrak measures the motion of the magnetic network pattern created by the dispersion of magnetic flux into the boundaries of convective cells. The MDI magnetograms used in this study have an image size of 1024×1024 and a 96-min cadence. MagTrak performs a cross-correlation analysis of long thin strips, (601×11 MDI heliographic projected pixels) centered on central meridian at 8-hour intervals. The overall displacement during that 8-hour interval is determined to within a fraction of a pixel, producing latitudinal and longitudinal velocities as a function of latitude. Several hundred

velocities from each 8-hour measurement over a 28-day period are then averaged to produce profiles of the differential rotation and meridional flow for every Carrington rotation during the MDI era, i.e., most of Solar Cycle 23. The average profiles are then used to produce *difference histories* that show key flow components: TO and active region inflows.

Rightmire-Upton, Hathaway, and Kosak (2012) adapted MagTrak for use with the larger 4096×4096 SDO/HMI magnetograms by binning them down to 1024×1024. They found that they could double the number of available cross-correlation data points by performing the cross-correlation both forward and backward in time. This analysis focused on the overlap period when both MDI and HMI were observing. They found that with HMI's better resolution, less noise, and more data, they were able to reduce the noise in the flow profiles significantly, particularly for the measurements nearest the poles (see Figures 2 and 3 of that paper).

Mahajan et al. (2021) have made several improvements to the magnetic pattern tracking algorithm, including: 1) broadening the search area to allow for better sampling of the Gaussian distribution of flow values; 2) correction of peak-locking errors inherent in the determination of motions to sub-pixel accuracy; 3) correction for the warping of tracked areas due to differential rotation; and 4) improved interpolation to reduce projection effects close to the limb. They analyzed full-resolution MDI (1024×1024) and full-resolution HMI (4096×4096) magnetograms, but rather than correlating long thin strips, they tracked blocks in order to get longitudinal coverage. This allowed them to characterize a systematic center-to-limb shift that appears as a pseudo-flow away from disk center, similar to one seen in helioseismology (Zhao et al., 2012a). They found that they could quantify and remove this shift by comparing displacements of the magnetic pattern measured at different time lags, further improving the results obtained by magnetic pattern tracking. They have made their measured baseline flow profiles as well as the center-to-limb error as a function of location on the solar disk available for every Carrington rotation (May 1996 – June 2020; Mahajan, 2021a,b). They found a TO pattern that agreed with helioseismic results. While they were not able to clearly see the poleward propagation of high-latitude branches, the alternating equatorward-propagating branches in the active latitudes were measured in great detail. They also noted that the equatorward-propagating branch that precedes the active regions of Solar Cycle 25, was very clearly visible. This dataset is referred to as MPT2 in this paper.

Hathaway, Upton, and Mahajan (2022) have implemented these improvements while keeping the long thin strips at a resolution of 1024×1024 pixels (binned HMI magnetograms). Results show that the improvements to MagTrak reduce the noise in the signal at low and mid-latitudes, despite lower input magnetogram resolution. In addition to the alternating equatorward-propagating branch in the torsional oscillation pattern, they noted a polar oscillation above $45°$ with a faster rotation during solar maxima and slower rotation during solar minima. They also noted that the equatorial variations were stronger in Cycle 24 than in Cycle 23, but the polar variations were weaker. In addition, they investigated flows at various depths within the surface shear layer by repeating the measurements with 2-hour and 4-hour time lags, with longer time lags corresponding to flows at greater depths (Hathaway, Upton, and Mahajan, 2022). It was found that the rotation rate increases inward, while no radial gradient was seen in the TO signal. Velocities obtained from this dataset are referred as MPT1 in this paper.
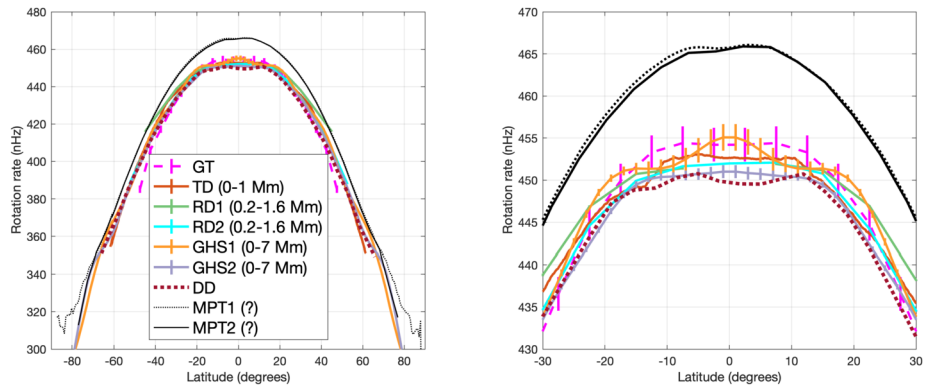
Figure 3 Mean differential rotation measured 22 Apr 2010 to 20 Jan 2011 (CR 2096 – 2105) obtained from measurements within 1 Mm of the surface using different techniques described in the text. (GT data is only available 16 Aug – 14 Sep 2010). Even though magnetic pattern tracking methods (MPT1 and MPT2) use surface magnetograms, their rotation profiles do not match other near-photosphere results.

4. Mean Differential Rotation During the MWO–GONG–MDI–HMI Overlap Period

4.1. Near-Surface

We compare the shape of the mean differential rotation profiles obtained by each technique between 22 April 2010 and 20 January 2011 (CR 2096 – 2105) in Figure 3. This time period is chosen because it represents the only interval with simultaneous observations from MWO, GONG, MDI, and HMI. The figure shows the mean differential rotation measurements in nHz in the sidereal frame from all techniques that provide data near the photosphere during this overlap period. For helioseismic inversions, we show data from the layer closest to the photosphere. Note that while most techniques show a similar rotation rate, MPT1 and MPT2 differ significantly, showing a significantly higher rotation rate at all latitudes. This is more easily seen in the right panel of Figure 3, which is a zoomed-in version of the left panel.

4.2. Depth Calibration of Magnetic Pattern Tracking

The MPT1 and MPT2 techniques that perform tracking on surface line-of-sight magnetograms infer a rotation rate that is not consistent with the near-surface rotation rate obtained by other techniques. This finding has been noticed previously in the pattern tracking analysis of supergranules in line-of-sight Dopplergrams by Hathaway (2012b). They attributed this difference to the depth at which supergranules are anchored. They found that supergranules of sizes ranging from 10 to 100 Mm moved with a rotation rate corresponding to a depth inside the Sun equal to their size visible on the photosphere. While supergranule sizes have a wide spectrum, their typical size was found to be 26 ± 2 Mm (see Table 1 of Hathaway (2012b) for a lag of 8 hours). Being anchored deeper inside the Sun, supergranules move with a rotation rate that conforms with the rotation rate of deeper layers. Mahajan et al. (2021) later improved the pattern-tracking algorithm, which improved the meridional flow results significantly, but didn't find any major systematic errors plaguing the measurements of differential rotation. So, we do not expect the above inferences to change.
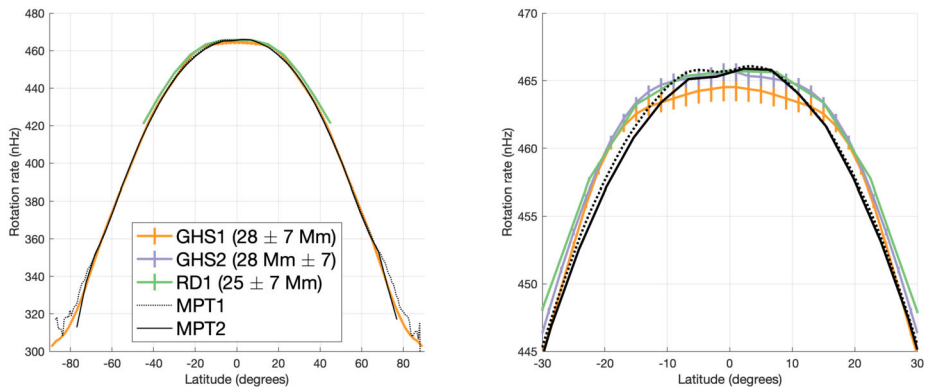
Figure 4 Angular rotation rates during the overlap period showing the depth at which differential rotation inferred from magnetic pattern tracking matches helioseismic inversions. For global helioseismology (HMI data), a match is found around 28 Mm whereas for ring diagram local helioseismology (GONG data) a match is found near 25 Mm.

We compare the mean differential rotation profile obtained from MPT1 and MPT2 with helioseismic rotation inversions from GHS1, GHS2 and RD1 (Figure 4) to find the depth at which they match. The best correspondence is found at depths 28 ± 7 Mm for GHS1 and GHS2, whereas the best match is at 25 ± 7 Mm with RD1. This result is consistent with the 26 ± 2 Mm found by Hathaway (2012b). It is therefore likely that, even if the magnetic pattern tracking technique utilizes surface magnetograms, the features actually track the rotation rate $\sim 25 – 28\ (\pm 7)$ Mm below the surface, which coincides with the typical size of supergranules and the depth at which they are anchored inside the Sun.

5. Torsional Oscillation in Solar Cycles 23 and 24

5.1. Comparison of Torsional Oscillation

Figure 5 shows the torsional oscillation (TO) pattern using different measurement techniques for Solar Cycles 23 and 24. Note that some of the observational techniques do not provide data over the whole analysis interval (5 May 1996 – 1 November 2020) or over all latitudes up to $\pm 70°$. The mean differential rotation for each of these data sets is calculated independently and is subtracted to reveal the residual variations in rotation rate with latitude and time, viz. torsional oscillation. This torsional oscillation signal has an amplitude $\sim 1\%$ of the average sidereal rotation rate and is well known to exhibit a period of 11 years, similar to the sunspot cycle (Howard and Labonte, 1980). Bands of faster-than-average and slower-than-average rotation rate originate around 60° latitude, propagate towards the equator, coincide with the activity belt of the upcoming cycle, before they merge and vanish near the equator ~ 24 years later (McIntosh et al., 2021). The physical mechanisms responsible for the spatio-temporal co-occurrence of torsional oscillation and the sunspot belt have hitherto been elusive. While there have been numerous candidates (Schuessler, 1981; Covas et al., 2000; Spruit, 2003; Rempel, 2007; Guerrero et al., 2016; Mahajan, 2019; Kosovichev and Pipin, 2019) consensus has not been reached yet. It is, therefore, necessary to extract properties of the TO pattern that are consistent across measurement techniques in order to provide useful constraints for models.
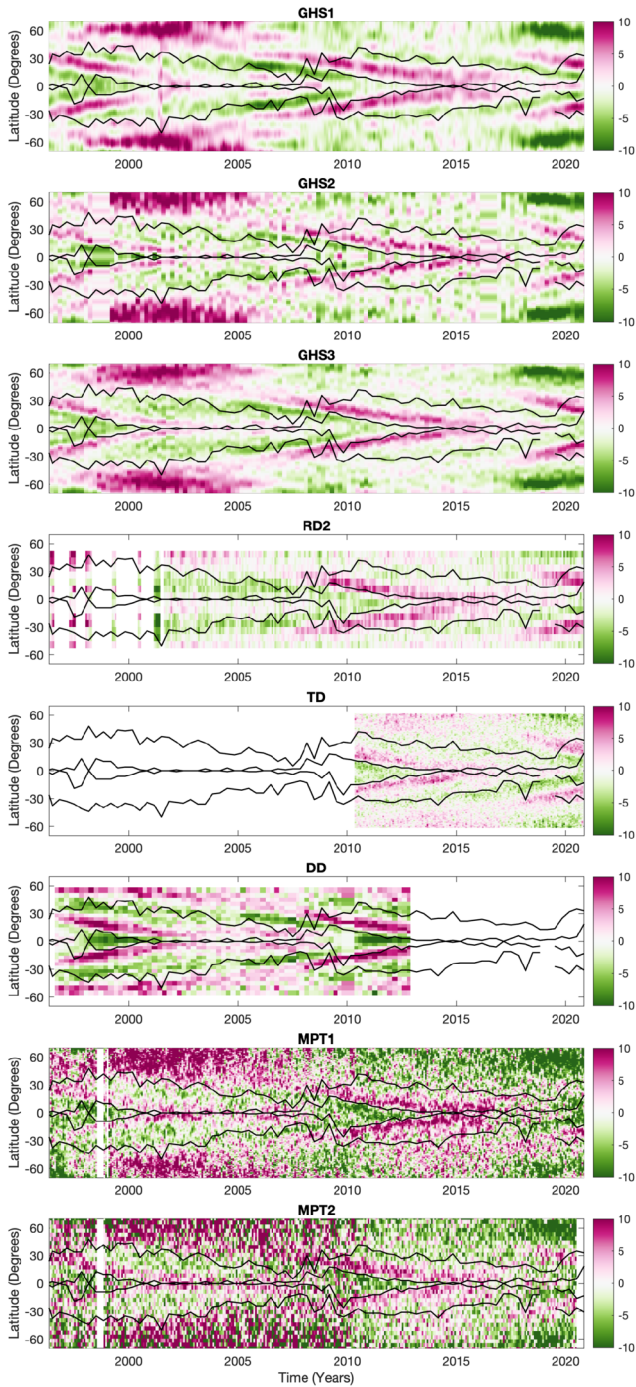
Figure 5 Torsional oscillation measurements (in ms^{-1}) in order from top to bottom: GHS1, GHS2, GHS3, RD2, TD, DD, MPT1, and MPT2 (refer to Table 2 for the acronyms). The solid black lines mark the sunspot belt derived from the RGO/NOAA database.

We find the following properties of the torsional oscillation pattern shown in Figure 5 are consistent across measurement techniques.

  i) The low-latitude side of the sunspot belt is comprised of a faster-than-average rotation-rate band, while the band poleward of the sunspot belt rotates more slowly (except in Cycle 24 for GHS1, where the bulk of the sunspot belt coincides with the faster band).

 ii) The faster-than-average rotation band that coincides with the sunspots of Cycle 24 originates around 1997, close to 60° latitude (a full solar cycle earlier).

iii) The origin of a similar, faster-than-average rotation band that would coincide with the sunspots of Cycle 25 cannot be seen around 60° latitude at the beginning of Cycle 24 (except in TD and DD, which show a weak, faster-than-average rotation band in 2010 around 60° latitude).

iv) The slower-than-average rotation band coinciding with sunspots in Cycle 24 originates in 2005 (except in MPT2 where the origin is plagued by noise), only 2 to 3 years preceding Cycle 24 around 60° latitude.

 v) A similar slower-than average rotation band is also seen originating around 2017 preceding Cycle 25 which is expected to coincide with the sunspots of Cycle 25 (except in MPT1 and MPT2, where the slower bands for Cycle 24 and Cycle 25 seem to mix together at high latitudes).

vi) At the highest latitudes, there are no obvious signs of an 11-year period in the TO except in measurements with the TD technique.

It is not surprising that in points #3 and #6, TD results show better indications of high-latitude TO branches. The primary reason is that among all the results shown in this figure, TD is the only one that shows only Cycle 24. It is well recognized that the mean differential rotation in Cycle 23 was different than Cycle 24 (Howe et al., 2013). Consequently, removing a 20-yr mean profile weakens the flows seen in Cycle 24 (Rempel, 2012); however, TD does not have measurements for Cycle 23 to average and remove, therefore the high-latitude bands are easily seen.

Comparing the TO pattern, which is constructed after subtracting independent background differential rotation profiles from each measurement, is like comparing voltages in circuits with independent floating grounds. The zero-level is different for each of the TO plots, and this can cause unknown biases to be identified as features. Therefore, we choose to calculate the acceleration, which both makes physical sense and has the added advantage of being independent of the mean differential rotation profile subtracted.

5.2. Comparison of Acceleration

In order to meaningfully compare the TO of the Sun, which have been measured on top of different mean differential rotation rates, we calculate the time derivative of TO, i.e., the acceleration. Such acceleration is independent of the background subtracted to reveal TO, and thus should facilitate meaningful comparison between measurements from various techniques. However, when one calculates the time derivative of a noisy measurement, the noise can overwhelm the signal in the calculated derivative, thus posing a challenge.

So, we first decompose the time varying rotation rate at each latitude into its associated Legendre coefficients (order $m = 1$, degrees 1 to 51). We then reconstruct the signal from the Legendre coefficients of the first six degrees at each latitude. This is essentially a smoothing operation like polynomial fitting, but it comes with minimal adverse edge effects that polynomial fitting largely suffers from. We then calculate the time derivative of this signal to infer the acceleration as a function of time at each latitude. In this way, we obtain

the acceleration plots shown in Figure 6 for all measurement techniques that have torsional oscillation data shown in Figure 5.

The acceleration/deceleration bands in Figure 6 that coincide with Cycle 24 begin at high latitudes about 20 years before they merge and vanish near the equator, confirming the major large-scale trend seen in torsional oscillation. The bulk of the sunspot belt is covered by deceleration regions (Mahajan, 2019; Kosovichev and Pipin, 2019) flanked by acceleration regions on the edges of the sunspot belt, with the low-latitude acceleration band penetrating the sunspot belt, while the high-latitude acceleration band lies outside of it. Properties #2, #4, and #5 of torsional oscillation described in the earlier section are consistent with this pattern of acceleration/deceleration bands. However, the analysis of the torsional oscillation misleads us for properties #3 (missing high-latitude origin of faster band prior to Cycle 24) and #6 (no clear 11-year period in high-latitude TO). The computation of acceleration in Figure 6 clearly reveals the high-latitude origin of bands that coincide with Cycle 24, and also unambiguously shows that the 11-year periodicity in the torsional oscillation exists even at high-latitudes $\sim 60°$. This was also noted by Howe et al. (2018). It also shows that the TO signature during Cycle 24 was much weaker than during Cycle 23. This suggests that the magnitude of the perturbation in TO is proportional to the strength of the sunspot cycle, which is a prediction common to all candidate theories that try to explain TO.

6. Conclusion

In order to better understand the solar dynamo and develop the capability of predicting aspects of the solar magnetic cycle, it is important to build a clear picture of the observations. The rotation rate of the Sun has been of interest ever since Christoph Schiener, along with Galileo, pointed his telescope at the Sun. Many methods can be used to measure the rate of differential rotation of the Sun, and each way has its own merits and demerits. Therefore, it is important to find and compare aspects of the solar differential rotation that are robust across the various measurement techniques.

While helioseismic, CST and DD measurement techniques are in agreement regarding the near-surface differential rotation of the Sun, magnetic pattern tracking differs significantly. Hathaway (2012a) establishes that this difference is due to supergranules being anchored deep inside the Sun and thus moving at non-surface speeds. We confirmed this by calibrating the rotation rates determined by MPT1 and MPT2 with the depth at which helioseismic measurements agree (25 to 28 Mm).

The TO pattern shows very similar qualitative features in relationship to the phase of the solar cycle, regardless of measurement technique used. However, a comparison of measurements of this essential solar periodic phenomenon is not straightforward due to the different sensitivities of each measurement, as well as to differences in the average rotation rate subtracted to obtain each of the TO measurements. A better, unbiased comparison can be made using the acceleration/deceleration derived from TO. While there is still quantitative disagreement across techniques, zones of deceleration coincide well with sunspot belts on the surface. The 11-year periodicity that is ambiguous in TO at high-latitudes becomes clearly evident in acceleration/deceleration. The relative amplitude of acceleration-deceleration was also weaker during Cycle 24 than in Cycle 23, suggesting a proportionality in the net azimuthal force and the strength of the sunspot cycle.

It remains to be seen whether the meridional flow, which is derived from varied measurement techniques, also exhibits such robust and consistent trends. We will address this in a follow-up paper.
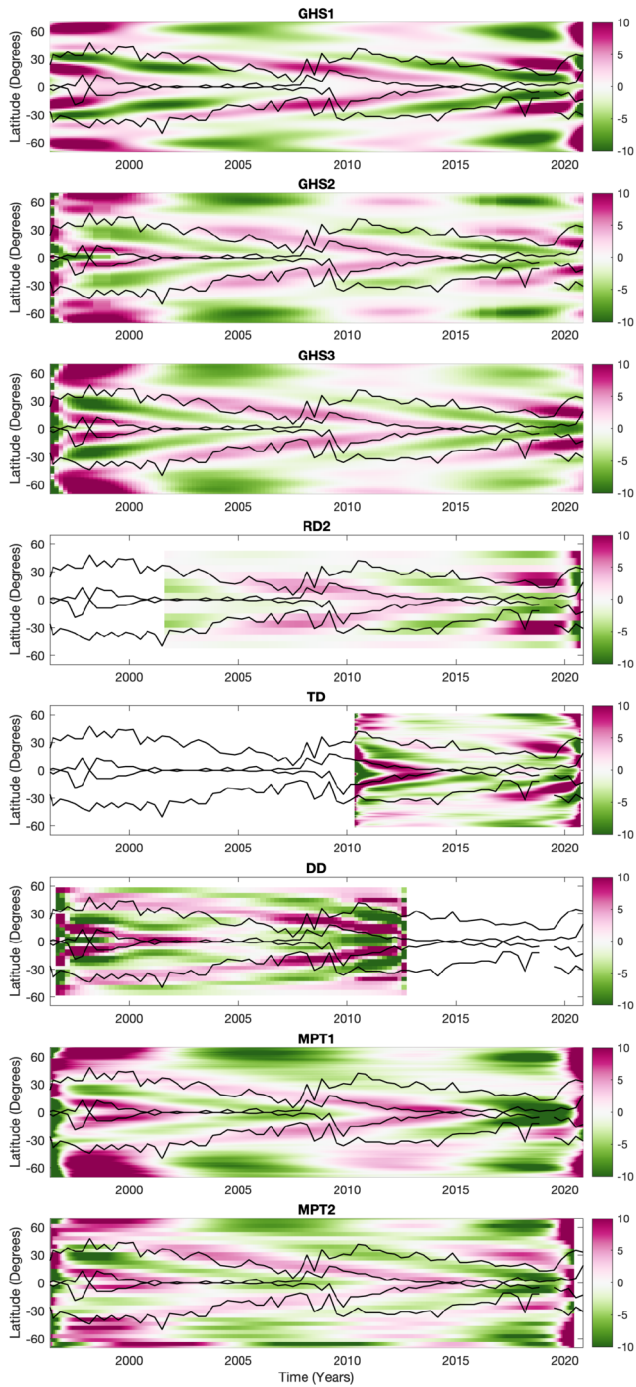
Figure 6 Acceleration in units of 10^{-8} m s^{-2} derived from torsional oscillation in order from top to bottom: GHS1, GHS2, GHS3, RD2, TD, DD, MPT1 and MPT2 (refer to Table 2 for the acronyms). The solid black lines mark the range of sunspot locations from the Royal Greenwich Observatory (RGO)/NOAA database.

Appendix: Rotation A Coefficients

Table 3 Rotational *A* coefficient averages over single Carrington rotations during the year 2010. Shown are the year value at the center of the average, the corresponding Carrington rotation number, the average of *A*, the number of observations, the rms of the *A* values, and the error of the mean for *A*. These are obtained with the direct Doppler technique from MWO observations.

Year	CR	A (μHz)	Nobs	A_{rms}	A_{EoM}
2010.2668861	2095.5	2.84637	8	2.17894E-03	8.23561E-04
2010.3415606	2096.5	2.84096	23	1.34176E-03	2.86063E-04
2010.4162351	2097.5	2.83596	24	1.80927E-03	3.77260E-04
2010.4909096	2098.5	2.84735	26	2.51393E-03	5.02785E-04
2010.5655840	2099.5	2.84374	27	2.20049E-03	4.31551E-04
2010.6402585	2100.5	2.84725	20	3.72394E-03	8.54331E-04
2010.7149330	2101.5	2.84811	27	2.74424E-03	5.38190E-04
2010.7896075	2102.5	2.83592	13	2.04269E-03	5.89674E-04
2010.8642819	2103.5	2.83932	19	2.25437E-03	5.31360E-04
2010.9389564	2104.5	2.84500	16	3.28507E-03	8.48201E-04

Data Availability Note that the data needed to recreate Figures 3 to 6 are available from Mahajan et al. (2024) or equivalently from doi.org/10.7910/DVN/7RLWAE.

Declarations

Competing interests   The authors declare no competing interests.

References

Adams, W.S.: 1911, An investigation of the rotation period of the Sun by spectroscopic methods. *Publ. Carnegie Inst. Washington* **138**, 1.

Antia, H.M., Basu, S.: 2022, Changes in the near-surface shear layer of the Sun. *Astrophys. J.* **924**, 19. DOI. ADS.

Antia, H.M., Basu, S., Chitre, S.M.: 1998, Solar internal rotation rate and the latitudinal variation of the tachocline. *Mon. Not. Roy. Astron. Soc.* **298**, 543. DOI. ADS.

Antia, H.M., Basu, S., Chitre, S.M.: 2008, Solar rotation rate and its gradients during cycle 23. *Astrophys. J.* **681**, 680. DOI. ADS.

Babcock, H.W.: 1953, The solar magnetograph. *Astrophys. J.* **118**, 387. DOI. ADS.

Babcock, H.W.: 1961, The topology of the Sun's magnetic field and the 22-YEAR cycle. *Astrophys. J.* **133**, 572. DOI. ADS.

Baldner, C.S., Schou, J.: 2012, Effects of asymmetric flows in solar convection on oscillation modes. *Astrophys. J. Lett.* **760**, L1. DOI. ADS.

Beckers, J.M., Nelson, G.D.: 1978, Some comments on the limb shift of solar lines. II - the effect of granular motions. *Solar Phys.* **58**, 243. ADS.

Belopolsky, A.: 1933, Bestimmung der Sonnenrotation auf spektroskopischem Wege in den Jahren 1931, 1932 und 1933 in Pulkovo. Mit 3 Abbildungen. *Z. Astrophys.* **7**, 357. ADS.

Bogart, R.S., Baldner, C., Basu, S., Haber, D.A., Rabello-Soares, M.C.: 2011a, HMI ring diagram analysis I. The processing pipeline. *J. Phys. Conf. Ser.* **271**, 012008. DOI. ADS.

Bogart, R.S., Baldner, C., Basu, S., Haber, D.A., Rabello-Soares, M.C.: 2011b, HMI ring diagram analysis II. Data products. *J. Phys. Conf. Ser.* **271**, 012009. DOI. ADS.

Carrington, R.C.: 1859, On certain phenomena in the motions of solar spots. *Mon. Not. Roy. Astron. Soc.* **19**, 81. DOI. ADS.

Chistiakov, V.F.: 1976, The rapid osciliations of the solar rotation. *Bull. Astron. Inst. Czechoslov.* **27**, 84. ADS.

Corbard, T., Toner, C., Hill, F., Hanna, K.D., Haber, D.A., Hindman, B.W., Bogart, R.S.: 2003, Ring-diagram analysis with GONG++. In: Sawaya-Lacoste, H. (ed.) *GONG+ 2002. Local and Global Helioseismology: The Present and Future*, ESA SP **517**, 255. ADS.

Covas, E., Tavakol, R., Moss, D., Tworkowski, A.: 2000, Torsional oscillations in the solar convection zone. *Astron. Astrophys.* **360**, L21. DOI. ADS.

Delury, R.E.: 1939, The law of solar rotation (with plate XIII). *J. Roy. Astron. Soc. Can.* **33**, 345. ADS.

Dravins, D., Lindegren, L., Nordlund, A.: 1981, Solar granulation - influence of convection on spectral line asymmetries and wavelength shifts. *Astron. Astrophys.* **96**, 345. ADS.

Duvall, J.T.L., Jefferies, S.M., Harvey, J.W., Pomerantz, M.A.: 1993, Time-distance helioseismology. *Nature* **362**, 430. DOI. ADS.

Galilei, G., Welser, M., de Filiis, A.: 1613, Istoria E dimostrazioni intorno alle macchie solari E loro accidenti comprese in tre lettere scritte all'illvstrissimo signor Marco Velseri.... ADS.

Guerrero, G., Smolarkiewicz, P.K., de Gouveia Dal Pino, E.M., Kosovichev, A.G., Mansour, N.N.: 2016, Understanding solar torsional oscillations from global dynamo models. *Astrophys. J. Lett.* **828**, L3. DOI. ADS.

Haber, D.A., Hindman, B.W., Toomre, J., Bogart, R.S., Thompson, M.J., Hill, F.: 2000, Solar shear flows deduced from helioseismic dense-pack samplings of ring diagrams. *Solar Phys.* **192**, 335. DOI. ADS.

Harvey, J., Tucker, R., Britanik, L.: 1998, High resolution upgrade of the GONG instruments. In: Korzennik, S. (ed.) *Structure and Dynamics of the Interior of the Sun and Sun-Like Stars*, *ESA Special Publication* **418**, 209. ADS.

Harvey, J.W., Hill, F., Hubbard, R.P., Kennedy, J.R., Leibacher, J.W., Pintar, J.A., Gilman, P.A., Noyes, R.W., Title, A.M., Toomre, J., Ulrich, R.K., Bhatnagar, A., Kennewell, J.A., Marquette, W., Patron, J., Saa, O., Yasukawa, E.: 1996, The Global Oscillation Network Group (GONG). *Project Sci.* **272**, 1284. DOI.

Hathaway, D.H.: 2012a, Supergranules as probes of solar convection zone dynamics. *Astrophys. J. Lett.* **749**, L13. DOI. ADS.

Hathaway, D.H.: 2012b, Supergranules as probes of the Sun's meridional circulation. *Astrophys. J.* **760**, 84. DOI. ADS.

Hathaway, D.H., Rightmire, L.: 2010, Variations in the Sun's meridional flow over a solar cycle. *Science* **327**, 1350. DOI. ADS.

Hathaway, D.H., Rightmire, L.: 2011, Variations in the axisymmetric transport of magnetic elements on the Sun: 1996 – 2010. *Astrophys. J.* **729**, 80. DOI. ADS.

Hathaway, D.H., Upton, L.A., Mahajan, S.S.: 2022, Variations in differential rotation and meridional flow within the Sun's surface shear layer 1996 – 2022. *Front. Astron. Space Sci.* **9**, 1007290. DOI. ADS.

Hathaway, D.H., Wilson, R.M.: 1990, Solar rotation and the sunspot cycle. *Astrophys. J.* **357**, 271. DOI. ADS.

Hill, F.: 1988, Rings and trumpets—three-dimensional power spectra of solar oscillations. *Astrophys. J.* **333**, 996. DOI. ADS.

Howard, R.: 1965, Introductory report. In: Lust, R. (ed.) *Stellar and Solar Magnetic Fields, IAU Symposium* **22**, 129. ADS.

Howard, R.: 1974, Studies of solar magnetic fields. I - the average field strengths. *Solar Phys.* **38**, 283. ADS.

Howard, R.: 1976, The Mount Wilson solar magnetograph: scanning and data system. *Solar Phys.* **48**, 411. DOI. ADS.

Howard, R., Boyden, J.E., Labonte, B.J.: 1980, Solar rotation measurements at Mount-Wilson - part one - analysis and instrumental effects. *Solar Phys.* **66**, 167. DOI. ADS.

Howard, R., Gilman, P.I., Gilman, P.A.: 1984, Rotation of the sun measured from Mount Wilson white-light images. *Astrophys. J.* **283**, 373. DOI. ADS.

Howard, R., Harvey, J.: 1970, Spectroscopic determinations of solar rotation. *Solar Phys.* **12**, 23. DOI. ADS.

Howard, R., Labonte, B.J.: 1980, The sun is observed to be a torsional oscillator with a period of 11 years. *Astrophys. J. Lett.* **239**, L33. DOI. ADS.

Howard, R., Tanenbaum, A.S., Wilcox, J.M.: 1968, A new method of magnetograph observation of the photospheric brightness, velocity, and magnetic fields. *Solar Phys.* **4**, 286. DOI. ADS.

Howard, R., Adkins, J.M., Boyden, J.E., Cragg, T.A., Gregory, T.S., Labonte, B.J., Padilla, S.P., Webster, L.: 1983a, Solar rotation results at Mount-Wilson - part four. *Results Solar Phys.* **83**, 321. DOI. ADS.

Howard, R., Boyden, J.E., Bruning, D.H., Clark, M.K., Crist, H.W., Labonte, B.J.: 1983b, The Mount Wilson magnetograph (report from a solar institute). *Solar Phys.* **87**, 195. DOI. ADS.

Howe, R., Christensen-Dalsgaard, J., Hill, F., Komm, R.W., Larsen, R.M., Schou, J., Thompson, M.J., Toomre, J.: 2000, Deeply penetrating banded zonal flows in the solar convection zone. *Astrophys. J. Lett.* **533**, L163. DOI. ADS.

Howe, R., Christensen-Dalsgaard, J., Hill, F., Komm, R., Larson, T.P., Rempel, M., Schou, J., Thompson, M.J.: 2013, The high-latitude branch of the solar torsional oscillation in the rising phase of cycle 24. *Astrophys. J. Lett.* **767**, L20. DOI. ADS.

Howe, R., Hill, F., Komm, R., Chaplin, W.J., Elsworth, Y., Davies, G.R., Schou, J., Thompson, M.J.: 2018, Signatures of solar cycle 25 in subsurface zonal flows. *Astrophys. J. Lett.* **862**, L5. DOI. ADS.

Jha, B.K., Priyadarshi, A., Mandal, S., Chatterjee, S., Banerjee, D.: 2021, Measurements of solar differential rotation using the century long kodaikanal sunspot data. *Solar Phys.* **296**, 25. DOI. ADS.

Komm, R., Howe, R., Hill, F.: 2018, Subsurface zonal and meridional flow during cycles 23 and 24. *Solar Phys.* **293**, 145. DOI. ADS.

Komm, R., González Hernández, I., Howe, R., Hill, F.: 2015, Subsurface zonal and meridional flow derived from GONG and SDO/HMI: a comparison of systematics. *Solar Phys.* **290**, 1081. DOI. ADS.

Kosovichev, A.G.: 1996, Tomographic imaging of the Sun's interior. *Astrophys. J. Lett.* **461**, L55. DOI. ADS.

Kosovichev, A.G., Pipin, V.V.: 2019, Dynamo wave patterns inside of the Sun revealed by torsional oscillations. *Astrophys. J. Lett.* **871**, L20. DOI. ADS.

Labonte, B.J., Howard, R.: 1982a, Are the high-latitude torsional oscillations of the sun real? *Solar Phys.* **80**, 373. DOI. ADS.

Labonte, B.J., Howard, R.: 1982b, Solar rotation measurements at Mount-Wilson - part three. *Meridional Flow and Limbshift. Solar Phys.* **80**, 361. DOI. ADS.

Lamb, D.A.: 2017, Measurements of solar differential rotation and meridional circulation from tracking of photospheric magnetic features. *Astrophys. J.* **836**, 10. DOI. ADS.

Larson, T.P., Schou, J.: 2015, Improved helioseismic analysis of medium-ℓ data from the Michelson Doppler imager. *Solar Phys.* **290**, 3221. DOI. ADS.

Larson, T.P., Schou, J.: 2018, Global-mode analysis of full-disk data from the Michelson Doppler imager and the helioseismic and magnetic imager. *Solar Phys.* **293**, 29. DOI. ADS.

Mahajan, S.S.: 2019, Observational constraints on the solar dynamo and the hunt for precursors to solar flares. PhD thesis, Georgia State University. ADS.

Mahajan, S.: 2021a, Level 3 photospheric flow measurements: longitudinally averaged f(latitude, time) DOI.

Mahajan, S.: 2021b, Level 4: fitted photospheric flow profiles for modelers DOI.

Mahajan, S.S., Hathaway, D.H., Muñoz-Jaramillo, A., Martens, P.C.: 2021, Improved measurements of the Sun's meridional flow and torsional oscillation from correlation tracking on MDI and HMI magnetograms. *Astrophys. J.* **917**, 100. DOI. ADS.

Mahajan, S.S., Upton, L.A., Antia, H.M., Basu, S., DeRosa, M.L., Hess Webber, S.A., Hoeksema, J.T., Jain, K., Komm, R.W., Larson, T., Nagovitsyn, Y.A., Pevtsov, A.A., Roudier, T., Tripathy, S.C., Ulrich, R.K., Zhao, J.: 2024, *Replication Data for: The Sun's Large-Scale Flows I: Measurements of Differential Rotation & Torsional Oscillation*. DOI.

McIntosh, S.W., Leamon, R.J., Egeland, R., Dikpati, M., Altrock, R.C., Banerjee, D., Chatterjee, S., Srivastava, A.K., Velli, M.: 2021, Deciphering solar magnetic activity: 140 years of the 'extended solar cycle' - mapping the Hale cycle. *Solar Phys.* **296**, 189. DOI. ADS.

Mitchell, W.M.: 1916, The history of the discovery of the solar spots. *Pop. Astron.* **24**, 206. ADS.

Nagovitsyn, Y.A., Pevtsov, A.A., Osipova, A.A.: 2018, Two populations of sunspots: differential rotation. *Astron. Lett.* **44**, 202. DOI. ADS.

Nagovitsyn, Y., Pevtsov, A., Osipova, A.: 2023a, Differential rotation for two populations of sunspots. DOI.

Nagovitsyn, Y., Pevtsov, A., Osipova, A.: 2023b, Two populations of sunspot groups and their meridional motions. *Solar Phys.* **298**, 108. DOI. ADS.

Newton, H.W., Nunn, M.L.: 1951, The Sun's rotation derived from sunspots 1934 – 1944 and additional results. *Mon. Not. Roy. Astron. Soc.* **111**, 413. DOI. ADS.

Parker, E.N.: 1955, Hydromagnetic dynamo models. *Astrophys. J.* **122**, 293. DOI. ADS.

Rempel, M.: 2007, Origin of solar torsional oscillations. *Astrophys. J.* **655**, 651. DOI. ADS.

Rempel, M.: 2012, High-latitude solar torsional oscillations during phases of changing magnetic cycle amplitude. *Astrophys. J. Lett.* **750**, L8. DOI. ADS.

Rightmire-Upton, L., Hathaway, D.H., Kosak, K.: 2012, Measurements of the Sun's high-latitude meridional circulation. *Astrophys. J. Lett.* **761**, L14. DOI. ADS.

Roudier, T., Rieutord, M., Malherbe, J.M., Renon, N., Berger, T., Frank, Z., Prat, V., Gizon, L., Švanda, M.: 2012, Quasi full-disk maps of solar horizontal velocities using SDO/HMI data. *Astron. Astrophys.* **540**, A88. DOI. ADS.

Roudier, T., Rieutord, M., Prat, V., Malherbe, J.M., Renon, N., Frank, Z., Švanda, M., Berger, T., Burston, R., Gizon, L.: 2013, Comparison of solar horizontal velocity fields from SDO/HMI and Hinode data. *Astron. Astrophys.* **552**, A113. DOI. ADS.

Roudier, T., Švanda, M., Ballot, J., Malherbe, J.M., Rieutord, M.: 2018, Large-scale photospheric motions determined from granule tracking and helioseismology from SDO/HMI data. *Astron. Astrophys.* **611**, A92. DOI. ADS.

Scheiner, C.: 1630, Rosa Ursina. DOI. ADS.

Scherrer, P.H., Bogart, R.S., Bush, R.I., Hoeksema, J.T., Kosovichev, A.G., Schou, J., Rosenberg, W., Springer, L., Tarbell, T.D., Title, A., Wolfson, C.J., Zayer, I., MDI Engineering Team: 1995, The solar oscillations investigation - Michelson Doppler imager. *Solar Phys.* **162**, 129. DOI. ADS.

Scherrer, P.H., Schou, J., Bush, R.I., Kosovichev, A.G., Bogart, R.S., Hoeksema, J.T., Liu, Y., Duvall, T.L., Zhao, J., Title, A.M., Schrijver, C.J., Tarbell, T.D., Tomczyk, S.: 2012, The Helioseismic and Magnetic Imager (HMI) investigation for the Solar Dynamics Observatory (SDO). *Solar Phys.* **275**, 207. DOI. ADS.

Schou, J., Christensen-Dalsgaard, J., Thompson, M.J.: 1994, On comparing helioseismic two-dimensional inversion methods. *Astrophys. J.* **433**, 389. DOI. ADS.

Schou, J., Antia, H.M., Basu, S., Bogart, R.S., Bush, R.I., Chitre, S.M., Christensen-Dalsgaard, J., Di Mauro, M.P., Dziembowski, W.A., Eff-Darwich, A., Gough, D.O., Haber, D.A., Hoeksema, J.T., Howe, R., Korzennik, S.G., Kosovichev, A.G., Larsen, R.M., Pijpers, F.P., Scherrer, P.H., Sekii, T., Tarbell, T.D., Title, A.M., Thompson, M.J., Toomre, J.: 1998, Helioseismic studies of differential rotation in the solar envelope by the solar oscillations investigation using the Michelson Doppler imager. *Astrophys. J.* **505**, 390. DOI. ADS.

Schou, J., Scherrer, P.H., Bush, R.I., Wachter, R., Couvidat, S., Rabello-Soares, M.C., Bogart, R.S., Hoeksema, J.T., Liu, Y., Duvall, T.L., Akin, D.J., Allard, B.A., Miles, J.W., Rairden, R., Shine, R.A., Tarbell, T.D., Title, A.M., Wolfson, C.J., Elmore, D.F., Norton, A.A., Tomczyk, S.: 2012, Design and ground calibration of the Helioseismic and Magnetic Imager (HMI) instrument on the Solar Dynamics Observatory (SDO). *Solar Phys.* **275**, 229. DOI. ADS.

Schuessler, M.: 1981, The solar torsional oscillation and dynamo models of the solar cycle. *Astron. Astrophys.* **94**, L17. ADS.

Snodgrass, H.B.: 1984, Separation of large-scale photospheric Doppler patterns. *Solar Phys.* **94**, 13. DOI. ADS.

Snodgrass, H.B., Howard, R.: 1985, Torsional oscillations of low mode. *Solar Phys.* **95**, 221. DOI. ADS.

Spruit, H.C.: 2003, Origin of the torsional oscillation pattern of solar rotation. *Solar Phys.* **213**, 1. DOI. ADS.

Stratonoff, W.: 1896, Rotation du Soleil déterminée par des facules. *Astron. Nachr.* **140**, 113. DOI. ADS.

Thompson, M.J., Toomre, J., Anderson, E.R., Antia, H.M., Berthomieu, G., Burtonclay, D., Chitre, S.M., Christensen-Dalsgaard, J., Corbard, T., De Rosa, M., Genovese, C.R., Gough, D.O., Haber, D.A., Harvey, J.W., Hill, F., Howe, R., Korzennik, S.G., Kosovichev, A.G., Leibacher, J.W., Pijpers, F.P., Provost, J., Rhodes, J.E.J., Schou, J., Sekii, T., Stark, P.B., Wilson, P.R.: 1996, Differential rotation and dynamics of the solar interior. *Science* **272**, 1300. DOI. ADS.

Tlatov, A.G., Pevtsov, A.A.: 2013, The effect of latitudinal averaging of surface tracers on patterns of torsional oscillations. In: Jain, K., Tripathy, S.C., Hill, F., Leibacher, J.W., Pevtsov, A.A. (eds.) *Fifty Years of Seismology of the Sun and Stars*, *Astronomical Society of the Pacific Conference Series* **478**, 297. ADS.

Ulrich, R.K., Tran, T., Boyden, J.E.: 2023, Photospheric velocities measured at Mt. Wilson show rotational and poleward velocity deviations compose the torsional oscillations. *Solar Phys.* **298**, 1. DOI.

Ulrich, R.K., Boyden, J.E., Webster, L., Snodgrass, H.B., Padilla, S.P., Gilman, P., Shieber, T.: 1988, Solar rotation measurements at MT. Wilson - part five. *Solar Phys.* **117**, 291. DOI. ADS.

Ulrich, R.K., Webster, L., Boyden, J.E., Magnone, N., Bogart, R.S.: 1991, A system for line profile studies at the 150-foot tower on Mount Wilson. *Solar Phys.* **135**, 211. DOI. ADS.

Ulrich, R.K., Evans, S., Boyden, J.E., Webster, L.: 2002, Mount Wilson synoptic magnetic fields: improved instrumentation, calibration, and analysis applied to the 2000 July 14 flare and to the evolution of the dipole field. *Astrophys. J. Suppl.* **139**, 259. DOI. ADS.

Vorontsov, S.V., Christensen-Dalsgaard, J., Schou, J., Strakhov, V.N., Thompson, M.J.: 2002, Helioseismic measurement of solar torsional oscillations. *Science* **296**, 101. DOI. ADS.

Zhao, J., Couvidat, S., Bogart, R.S., Parchevsky, K.V., Birch, A.C., Duvall, T.L., Beck, J.G., Kosovichev, A.G., Scherrer, P.H.: 2012b, Time-distance helioseismology data-analysis pipeline for helioseismic and magnetic imager onboard solar dynamics observatory (SDO/HMI) and its initial results. *Solar Phys.* **275**, 375. DOI. ADS.

Zhao, J., Nagashima, K., Bogart, R.S., Kosovichev, A.G., Duvall, J.T.L.: 2012a, Systematic center-to-limb variation in measured helioseismic travel times and its effect on inferences of solar interior meridional flows. *Astrophys. J. Lett.* **749**, L5. DOI. ADS.

Authors and Affiliations

Sushant S. Mahajan[1] ⓘ · **Lisa A. Upton**[2] ⓘ · **H.M. Antia**[3] ⓘ · **Sarbani Basu**[4] ⓘ ·
Marc L. DeRosa[5] ⓘ · **Shea A. Hess Webber**[1] ⓘ · **J. Todd Hoeksema**[1] ⓘ · **Kiran Jain**[6] ⓘ ·
Rudolf W. Komm[6] ⓘ · **Tim Larson** ⓘ · **Yury A. Nagovitsyn**[7] ⓘ · **Alexei A. Pevtsov**[6] ⓘ ·
Thierry Roudier[8] ⓘ · **Sushanta C. Tripathy**[6] ⓘ · **Roger K. Ulrich**[9] ⓘ · **Junwei Zhao**[1] ⓘ

✉ S.S. Mahajan
   mahajans@stanford.edu

1   W.W. Hansen Experimental Physics Laboratory, Stanford University, Stanford, CA 94305, USA

2   Southwest Research Institute, Boulder Office, 1050 Walnut St, Suite 300, Boulder, CO 80302, USA

3   UM-DAE Centre of Excellence for Basic Sciences, University of Mumbai, Kalina, Mumbai 400098, India

4   Department of Astronomy, Yale University, PO Box 208101, New Haven, CT 06520-8101, USA

5   Lockheed Martin Solar and Astrophysics Laboratory, 3176 Porter Dr, Palo Alto, CA 94304, USA

[6]   National Solar Observatory, 3665 Discovery Dr., Boulder, CO 80303, USA

[7]   Central Astronomical Observatory at Pulkovo, St. Petersburg, 196140, Russia

[8]   IRAP/Observatoire Midi-Pyrénées, 14, avenue Edouard Belin, 31400 Toulouse, France

[9]   Department of Physics and Astronomy, UCLA, Los Angeles, CA, 90095-1547, USA